Research Square

Preprints are preliminary reports that have not undergone peer review.
They should not be considered conclusive, used to inform clinical practice,
or referenced by the media as validated information.

Fracture Propagation Analysis of Limited-Entry Perforation in Horizontal Multi-Cluster Fracturing Considering Thermal Effects

Hao Jiang

jianghao27@foxmail.com

PetroChina Southwest Oil & Gas Field

Jianfeng Xiao

PetroChina Southwest Oil & Gas Field

Wei Jiang

PetroChina Southwest Oil & Gas Field

Liang Yang

PetroChina Southwest Oil & Gas Field

Lan Ren

Southwest Petroleum University

Cai Deng

PetroChina Southwest Oil & Gas Field

Dengji Tang

PetroChina Southwest Oil & Gas Field

Longqing Zou

PetroChina Southwest Oil & Gas Field

Article

Keywords: deep shale, hydraulic fracturing, multi-fracture propagation, thermal effect, limited-entry perforation fracturing, displacement discontinuity method

Posted Date: October 12th, 2026

DOI: https://doi.org/10.21203/rs.3.rs-10834409/v1

License: This work is licensed under a Creative Commons Attribution 4.0 International License.
Read Full License

Additional Declarations: No competing interests reported.

Version of Record: A version of this preprint was published at Scientific Reports on November 13th, 2026. See the published version at https://doi.org/10.1038/s41598-026-80496-z.

Fracture Propagation Analysis of Limited-Entry Perforation in Horizontal Multi-Cluster Fracturing Considering Thermal Effects

Hao Jiang [a,*], Jianfeng Xiao [a], Wei Jiang [a], Liang Yang [a], Lan Ren [b], Cai Deng [a], Dengji Tang [a], Longqing, Zou[a]

a. PetroChina Southwest Oil & Gas Field, Chengdu, Sichuan, 610051, China

b. State Key Laboratory of Oil & Gas Reservoir Geology and Exploitation in Southwest Petroleum University, Chengdu 610500, China

Abstract: The long-stage multi-cluster fracturing process is widely applied in the development of deep shale reservoirs, but it also faces the challenge of non-equilibrium propagation of multiple fractures. The mechanism of the temperature disturbance caused by the injection of low-temperature fracturing fluid into deep high-temperature formations and the resulting thermal effect on the competitive extension of multi-cluster fractures has not yet been clarified. To reveal the influence of thermal effect on the competitive propagation of multi-cluster fractures, based on the finite volume method and displacement discontinuity method, a numerical model for non-planar fracture propagation in multi-stage multi-cluster fracturing considering thermal effect was established. The simulation and analysis of the limited-entry perforation fracturing under the action of thermal effects was carried out. The perforation numbers were optimized under different geological conditions. The results show that the thermal effect intensifies the non-equilibrium extension of multi-cluster fractures. When the formation temperature increases from 60 ℃ to 180 ℃, the dimensionless length variation coefficient L_{cv} increases from 0.28 to 0.61, and the standard deviation of the transient inflow ratio Q_{sd} increases from 6.82%. to 12.29%; Maintaining the perforation friction at 3.3 MPa~7.5 MPa can eliminate to a certain extent the non-equilibrium propagation caused by the given heterogeneous ground stress, stress shadow between fractures and thermal effects; The optimal number of perforations decreases with the increase of Young's modulus and increases with the increase of pumping rate. Increasing the pumping rate can relatively weaken the negative impact of thermal effects on the balanced inlet of each cluster. The study shows that thermal effects have an important impact on fracture propagation when the underground temperature is higher than 90 °C. The research results can provide a more comprehensive reference for deep shale fracturing design.

Key words: deep shale; hydraulic fracturing; multi-fracture propagation; thermal

effect; limited-entry perforation fracturing; displacement discontinuity method

Introduction

China possesses vast deep oil and gas resources with wide distribution. Taking the Upper Ordovician Wufeng Formation-Lower Silurian Longmaxi Formation in southern Sichuan as an example, its deep shale gas reserves reach 6.6×10^{12} m^3. Therefore, deep shale gas serves as a critical energy alternative for unconventional gas production However, complex geomechanics conditions in deep shale reservoirs increase fracture turning difficulty and complicate fracture network construction. While high-density, long-stage multi-cluster fracturing technology is widely applied, it faces challenges of unbalanced multi-fracture propagation. Additionally, temperature disturbances caused by injecting low-temperature fracturing fluids into deep high-temperature formations introduce thermal effects, adding uncertainties to multi-cluster fracture competition and often failing to achieve expected stimulation effects [1].

Studies on fracture deformation and propagation under thermal effects have been conducted. Ghassemi et al [2]. used a 3D thermo-poroelastic model to analyze transient temperature, pressure, and aperture distributions in static pressurized fractures in enhanced geothermal systems. Wang [3] and Lu et al. [4] studied the formation mechanisms and propagation laws of secondary fractures considering fluid-solid coupling. Abollahipour et al. [5] proposed a thermo-poroelastic DDM method to investigate thermal-fluid-solid coupling effects on fracture apertures. However, these studies primarily focused on geometric evolution of static main fractures, temperature/stress evolution of solids/fluids, and secondary fracture propagation, without addressing hydraulic fracture extension. Tarasovs and Ghassemi [6] studied micro-fracture propagation near wellbores under thermal shock. Li et al. [7] demonstrated that thermal stress promotes fracture initiation and extension using discrete element methods, while Salimzadeh et al. [8] found minimal thermal effects on fracture formation using linear elasticity and 3D FEM. Bazargan et al. [9] concluded that thermal stress alone cannot drive fracture propagation but reduces resistance required for initiation, a finding corroborated by Siemann et al. Luo et al. [10] showed that thermal stress increases fracture width and reduces fluid pressure using XFEM, with Liu et al. [11] reaching similar conclusions regarding non-isothermal fluids.

Despite progress in understanding thermal stress effects on single-fracture

mechanisms, the competition laws of multi-cluster fractures under thermal effects remain unclear. Revealing these competition laws and proposing optimization measures for fracture spatial distribution are crucial for economically efficient deep shale development. This study establishes a numerical model for multi-stage multi-cluster fracturing with non-planar fractures using finite volume and displacement discontinuity methods, simulating and analyzing thermal effects on horizontal well limited-entry perforation fracturing to optimize perforation numbers under different geological conditions.

1 Mathematical framework

1.1 Governing equations of fluid flow

Flow in wellbore. The wellbore flow is characterized by two key principles: mass conservation within the wellbore and pressure balance. Neglecting the wellbore storage effect, the total flow rate in the wellbore equals the sum of the flow rates distributed among each cluster fracture. The pressure at the wellbore heel is equal to the sum of the frictional pressure drop within the wellbore, the perforation frictional pressure drop, and the fracture entry pressure. Accordingly, the governing equations for wellbore flow are established as follows:

$$\begin{cases} Q_T = \sum_{k=1}^{N_\mathrm{f}} Q_k \\ p_\mathrm{in} = p_{\mathrm{w},k} + p_{\mathrm{pf},k} + p_{\mathrm{wf},k},\ k = 1,...,N_\mathrm{f} \end{cases} \tag{1}$$

And $\boldsymbol{p_{\mathrm{pf},k}}$ and $\boldsymbol{p_{\mathrm{wf},k}}$ are respectively calculated by the eq(2) and eq(3):

$$p_{\mathrm{pf},k} = \frac{0.2369\rho_f}{n_{\mathrm{pf},k}^2 d_{\mathrm{pf},k}^4 K_\mathrm{d}^2} Q_k^2 \tag{2}$$

$$P_{\mathrm{wf},k} = \frac{128\mu}{\pi d_\mathrm{w}^4} \sum_{j=1}^{k} L_{\mathrm{w},k} \left(Q_T - \sum_{j=1}^{k-1} Q_j \right) \tag{3}$$

Where $\boldsymbol{Q_T}$ is the total flow rate of the fracturing fluid, m³/s; $\boldsymbol{Q_k}$ is the injection flow rate into fracture k, m³/s; $\boldsymbol{p_{in}}$ is the pressure at the heel of the wellbore, Pa; $\boldsymbol{p_{w,k}}$ is the pressure at the entrance of the k-th fracture, Pa; $\boldsymbol{p_{pf,k}}$ is the perforation friction pressure of the k-th fracture, Pa; $\boldsymbol{p_{wf,k}}$ is the flow friction pressure inside the horizontal wellbore section between the k-th fracture and the (k−1)-th fracture (for k = 2,…, N_f), Pa; when k=1, $\boldsymbol{p_{wf,1}}$ is the flow friction pressure over the distance from the heel of the wellbore to the first fracture; $\boldsymbol{\mu}$ is the viscosity, Pa·s; $\boldsymbol{n_{pf,k}}$ is the number of perforation holes in the k-th fracture, dimensionless; $\boldsymbol{d_{pf,k}}$ is the diameter of the perforation holes in the

k-th fracture, m; K_d is the perforation flow coefficient, dimensionless; ρ_f is the density of the fracturing fluid, kg/m³; d_w is the diameter of the wellbore, m; $L_{w,k}$ is the length of the *k*-th horizontal wellbore section, m.

Flow in Fracture. The flow within the fracture is described by Poiseuille's law. Based on the filtration theory model of fracturing fluid [12]] and the exponential viscosity-temperature relationship [13], the governing equations for fluid flow within the fracture, accounting for temperature-sensitive dynamic filtration, are as follows:

$$\frac{\partial w}{\partial t}+\nabla\cdot q+\frac{2C_{\text{leak}}}{\sqrt{t-\tau(x)}}=\delta\left(\boldsymbol{x}-\boldsymbol{x}_{\text{in},k}\right)q_k \tag{4}$$

$$C_{\text{leak}}=\frac{C_{\text{leak}}^{0}}{\sqrt{\exp\left(-C_T\left(T-T_0\right)\right)}} \tag{5}$$

$$q=-\frac{w^3}{12u}\nabla p \tag{6}$$

Where q is the volumetric flow rate of the fracturing fluid within the fracture, m²/s; w is the fracture width, m; p is the pressure inside the fracture, Pa; t is the time, s; $\delta(x-x_{\text{in}})$ is the Dirac delta function representing the injection point source at x_{in}, dimensionless; q_k is the injection flow rate per unit area of the *k*-th fracture, m/s; C_{leak} is the filtration coefficient, m·s$^{1/2}$; C_{leak}^{0} is the filtration coefficient at the reference temperature T_0, m·s$^{1/2}$; C_T is the temperature-sensitive coefficient, 1/°C; $\tau(x)$ is the time at which the fluid arrives at location x within the fracture, s; T is the temperature at the simulation time, °C.

1.2 **Governing equations of temperature**

The temperature field calculation for multi-cluster fractures is based on the classical KDR model [14] and incorporates the assumption that the temperature distributions between adjacent fractures are mutually independent. This is because the zone of temperature variation in the near-fracture formation is less than 1 m, whereas in current engineering practice, the cluster spacing in multi-cluster fracturing remains greater than 5 m. A schematic diagram of the heat transfer process in staged fracturing is shown in Fig. 1.

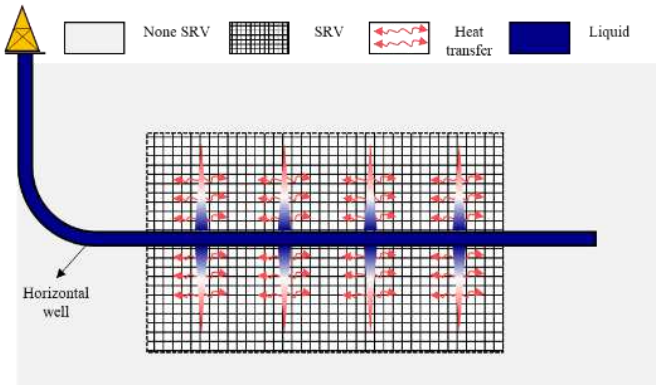


Fig.1 Schematic diagram of the heat transfer process in multi-staged fracturing

Energy conservation equation in the fracture. Assuming the fracturing fluid within the fracture is incompressible, the fracture is divided into multiple micro-elements. In each micro-element, the rate of change of fluid temperature with time equals the difference between the incoming and outgoing heat flow rates. Accordingly, the energy conservation equation for the fluid within the fracture can be expressed as:

$$w\frac{\partial T_{\mathrm{f}}}{\partial t}=-wV_{\mathrm{f}}\frac{\partial T_{\mathrm{f}}}{\partial x}+\frac{2\alpha_{\mathrm{T}}}{\rho_{\mathrm{f}}c_{\mathrm{f}}}\left(T_{\mathrm{fw}}-T_{\mathrm{f}}\right) \tag{10}$$

Where $\boldsymbol{V_f}$ is the fluid velocity under the average fracture width, m/s; $\boldsymbol{T_f}$ is the temperature of the fluid within the fracture, °C; $\boldsymbol{\rho_f}$ is the fluid density, kg/m³; $\boldsymbol{c_f}$ is the specific heat capacity of the fluid, J/(kg·°C); $\boldsymbol{T_{fw}}$ is the temperature of the fracture wall, °C; $\boldsymbol{\alpha_T}$ is the heat transfer coefficient, W/(m²·°C), and its calculation is referred to in references [14].

Energy conservation equation for the fracture wall. The temperature variation of the fracture wall is governed by heat conduction on the rock side, as well as heat conduction and heat convection on the fluid side. The corresponding energy conservation equation is as follows:

$$\frac{\partial T_{\mathrm{fw}}}{\partial t}=\frac{1}{\delta}\left[\frac{\rho_{\mathrm{f}}c_{\mathrm{f}}}{(\rho c)_{\mathrm{eff}}}V_{\mathrm{leak}}\left(T_{\mathrm{f}}-T_{\mathrm{fw}}\right)+\frac{\alpha_{\mathrm{T}}}{(\rho c)_{\mathrm{eff}}}\left(T_{\mathrm{f}}-T_{\mathrm{fw}}\right)+\frac{k_{\mathrm{ef}}}{(\rho \mathrm{c})_{\mathrm{eff}}}\frac{\partial T_{\mathrm{r}}}{\partial y}\bigg|_{y=0}\right] \tag{11}$$

And V_{leak}, k_{eff} and $(\rho c)_{\mathrm{eff}}$ are respectively calculated by the eq(8) and eq(12):

$$V_{\mathrm{leak}}=\frac{C_{\mathrm{leak}}}{\sqrt{t-\tau(x)}} \tag{8}$$

$$\begin{aligned}k_{\mathrm{eff}}&=\phi k_{\mathrm{f}}+(1-\phi)k_{\mathrm{r}}\\(\rho c)_{\mathrm{eff}}&=\phi\rho_{\mathrm{f}}c_{\mathrm{f}}+(1-\phi)\rho_{\mathrm{r}}c_{\mathrm{r}}\end{aligned} \tag{12}$$

Where $\boldsymbol{\delta}$ is the thickness of the filtration zone, m (since the thickness of the filtration

zone is extremely small, its temperature gradient is neglected) ; k_{eff} is the effective thermal conductivity coefficient of the porous medium, W/(m·°C); V_{leak} is the filtration velocity, m/s; $(\rho c)_{eff}$ is the product of the effective specific heat capacity and density of the fluid and rock; ϕ is the porosity of the rock, %; k_f is the thermal conductivity coefficient of the fluid, W/(m·°C); k_r is the thermal conductivity coefficient of the formation rock, W/(m·°C); ρ_r is the density of the formation rock, kg/m³; c_r is the specific heat capacity of the formation rock, J/(kg·°C); T_r is the temperature of the formation rock, °C; y is the vertical distance from any point to the fracture wall, m.

Energy conservation equation for the formation. The energy variation in the formation rock is directly related to the heat transfer from the formation to the fracture wall, which in turn exchanges heat with the fluid within the fracture. Based on the principle of thermal equilibrium, the energy equation for the formation rock is as follows:

$$\frac{\partial T_{\mathrm{r}}}{\partial t}=\frac{k_{\mathrm{eff}}}{(\rho c)_{\mathrm{eff}}}\frac{\partial^{2} T_{\mathrm{r}}}{\partial y^{2}}-\frac{\rho_{\mathrm{f}}\mathrm{c}_{\mathrm{f}}}{(\rho c)_{\mathrm{eff}}}V_{\mathrm{leak}}\frac{\partial T_{\mathrm{r}}}{\partial y} \tag{13}$$

The initial and boundary conditions for the governing equation of the temperature field are as follows:

$$\begin{cases} T=T_{\mathrm{res}}, & (t=0, x>0, y\geq 0) \\ T=T_{\mathrm{res}}, & (\mathrm{t}<\mathrm{t}_{\mathrm{pump}}, x\geq 0, y=y_{\max}) \\ T=T_{\mathrm{fini}}, & (0<\mathrm{t}<\mathrm{t}_{\mathrm{pump}}, \mathrm{x}=0, \mathrm{y}=0) \end{cases} \tag{14}$$

Where T_{res} is the original formation temperature, °C; T_{fini} is the fluid temperature at the fracture entry, °C; t_{pump} is the pumping time, s; y_{max} is the maximum heat transfer distance perpendicular to the fracture plane, m.

1.3 Governing equations for solid deformation

Governing equation. The elastic deformation behavior of rock can be described using the Displacement Discontinuity Method (DDM) proposed by Crouch [15]. For fracture problems, the fracture surface is taken as the boundary and discretized into N elements of equal length (as illustrated in Figure 2). According to the DDM formulation, the normal stress σ_n^i and shear stress σ_s^i acting on an arbitrary fracture element i can be expressed as:

$$\left.\begin{aligned}\sigma_s^i &= \sum_{j=1}^{N} G^{ij} A_{ss}^{ij} D_s^j + \sum_{j=1}^{N} G^{ij} A_{sn}^{ij} D_n^j \\ \sigma_n^i &= \sum_{j=1}^{N} G^{ij} A_{ns}^{ij} D_s^j + \sum_{j=1}^{N} G^{ij} A_{nn}^{ij} D_n^j\end{aligned}\right\}, \quad i = 1,2,...,N \tag{16}$$

Where $\boldsymbol{A_{ij}^{ss}}$, $\boldsymbol{A_{ij}^{sn}}$, $\boldsymbol{A_{ij}^{ns}}$, and $\boldsymbol{A_{ij}^{nn}}$ are the elastic stress–strain influence coefficients, the expressions of which are referred to in the literature [15]; $\boldsymbol{D_j^n}$ and $\boldsymbol{D_j^s}$ represent the normal and shear displacement discontinuities of fracture element $\boldsymbol{j}$, respectively, in meters; and $\boldsymbol{G_{ij}}$ is the fracture height correction factor, the calculation of which follows Olson et al. [16]。

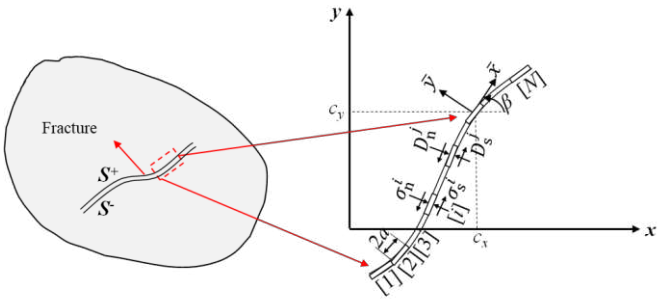


Fig. 2 Schematic diagram of arbitrary fracture discretization

Stress boundary. In the local coordinate system $\boldsymbol{s_i - n_i}$ of fracture element $\boldsymbol{i}$, the stress boundary condition is collectively determined by the fluid pressure $\boldsymbol{p_f}$ within the fracture, the far-field in-situ stresses $\boldsymbol{(\sigma_x^\infty, \sigma_y^\infty, \tau_{xy}^\infty)}$, and the thermal stress $\boldsymbol{\sigma_{\Delta T}}$. It can be expressed as:

$$\left.\begin{aligned}\sigma_n^i &= P_f^i - \sigma_n^{\infty i} - \sigma_{\Delta T}^i \\ \sigma_s^i &= -\sigma_s^{\infty i}\end{aligned}\right\}, \quad i = 1,2,...,N \tag{20}$$

Where $\boldsymbol{P_i^f}$ is the fluid pressure in fracture element i, Pa; $\boldsymbol{\sigma_{n,i}^\infty}$ and $\boldsymbol{\tau_i^\infty}$ are the normal and shear stress components, respectively, of the far-field in-situ stress field acting on fracture element i in the local coordinate system $\boldsymbol{s_i}$–$\boldsymbol{n_i}$, Pa; and $\boldsymbol{\sigma_{\Delta T}}$ is the thermal stress acting on the fracture element, Pa.

The normal and shear stresses ($\boldsymbol{\sigma_{n,i}^\infty}$, $\boldsymbol{\tau_i^\infty}$) of the far-field in-situ stress field at fracture element i in the local coordinate system $s_i - n_i$ are expressed as:

$$\left.\begin{aligned}\sigma_n^{\infty i} &= \sigma_{\mathrm{H}} \sin^2 \gamma_i + \sigma_{\mathrm{h}} \cos^2 \gamma_i \\ \sigma_s^{\infty i} &= (\sigma_{\mathrm{h}} - \sigma_{\mathrm{H}}) \sin \gamma_i \cos \gamma_i\end{aligned}\right\}, \quad i = 1,2,...,N_f * N \tag{18}$$

Where $\boldsymbol{\sigma_H}$ and $\boldsymbol{\sigma_h}$ are the maximum and minimum horizontal principal stresses, Pa;

$\boldsymbol{\gamma_i}$ is the angle between fracture element $\boldsymbol{i}$ and the global x-axis, °.

The thermal stress $\boldsymbol{\sigma_{\Delta T}}$ acting on the fracture element can be calculated by the following equation[17]:

$$\sigma_{\Delta T}=\frac{E\alpha_{\mathrm{e}}}{1-\nu}\left(T_{\mathrm{fnear}}-T_0\right)f \tag{19}$$

Where $\boldsymbol{E}$ is the elastic modulus of the rock, Pa; $\boldsymbol{\alpha_e}$ is the thermal expansion coefficient of the rock, °C^{-1}; $\boldsymbol{T_{\mathrm{fnear}}}$ is the temperature at the center of the element near the fracture, °C; $\boldsymbol{T_0}$ is the reference temperature, °C; and $\boldsymbol{f}$ is a coefficient related to the cooling region, the calculation of which is described in the literature[18]. $\boldsymbol{f}$ is taken as 0.7 in this study.

1.4 **Fracture propagation criterion**

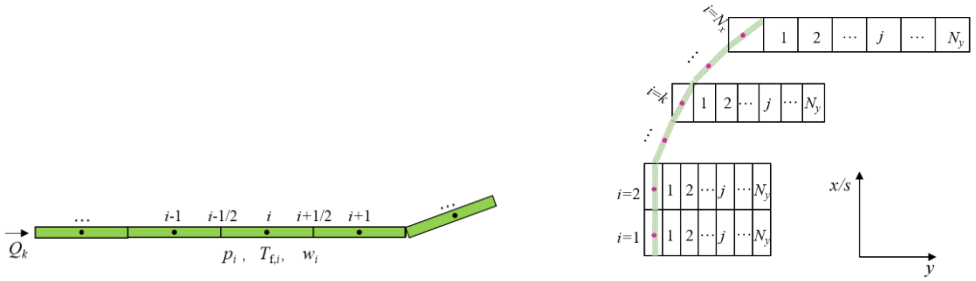
Fracture propagation is governed by the fracture mechanics at the tip, and the F-criterion, which is applicable to mixed-mode propagation, is adopted as the propagation criterion[19]. Its expression is given as:

$$F\left(\theta\right)=\frac{G_{\mathrm{I}}\left(\theta\right)}{G_{\mathrm{Ic}}}+\frac{G_{\mathrm{II}}\left(\theta\right)}{G_{\mathrm{IIc}}},\ G_i\left(\theta\right)=\frac{\left(1-\nu^2\right)}{E}K_{ie}^2 \tag{21}$$

Where $\boldsymbol{G_I(\theta)}$ and $\boldsymbol{G_{II}(\theta)}$ are the energy release rates for Mode I and Mode II fractures in the θ direction, respectively, Pa·m; $\boldsymbol{G_{Ic}}$ and $\boldsymbol{G_{IIc}}$ are the critical energy release rates for Mode I and Mode II fractures, respectively, Pa·m; $\boldsymbol{K_I^e}$ and $\boldsymbol{K_{II}^e}$ are the equivalent stress intensity factors for Mode I and Mode II fractures, respectively, Pa·m$^{0.5}$. The detailed calculation can be found in the reference [15].

2 Numerical solution methods

Using the displacement discontinuity method requires discretizing only the fractures, which reduces the computational dimension. Therefore, the fluid control equations within the fracture, as well as the energy control equations within the fracture and on the fracture walls, are discretized using the same set of mesh (as shown in Figure 3a). For solving the formation heat exchange, a box-type grid is adopted for the formation mesh (as shown in Figure 3b). Since a large number of fracture propagation results indicate that the fracture deflection is extremely small when the horizontal stress difference exceeds 2 MPa, and the formation heat exchange considered in this paper is only one-dimensional heat transfer, the error introduced by using the temperature gradient normal to the fracture as the temperature gradient along the y-axis is negligible in this case.



(a) Schematic diagram of discrete fracture units

(b) Grid and element numbering of non-planar fractured formation

Fig. 3 Schematic diagram of discretization for fractures and formation

To discretize the governing equations for fluid flow within the fracture, the finite volume method is applied, using fracture element *i* as a representative example:

$$\begin{aligned} w_i^n - w_i^{n-1} = \Delta t \left[\frac{1}{\Delta x} \left(\frac{\left(w_{i+1/2}^n\right)^3}{\mu'} \frac{p_{i+1}^n - p_i^n}{\Delta x} - \frac{\left(w_{i-1/2}^n\right)^3}{\mu'} \frac{p_i^n - p_{i-1}^n}{\Delta x} \right) \right] \\ - 4C_{\text{leak}}^i \left(\sqrt{t + \Delta t - \tau\left(x_i\right)} - \sqrt{t - \tau\left(x_i\right)} \right) + \frac{Q_k}{\Delta x h} \delta \end{aligned} \tag{22}$$

Where w_i^n and w_i^{n-1} are the fracture widths of element ***i*** at the current time step and the previous time step, respectively, and **Δ*t*** is the time step size.

To guarantee numerical stability, the energy equation governing the fluid inside the fracture and that governing the fracture walls are discretized using the implicit first-order upwind scheme：

$$w_i^n \frac{T_{\text{f},i}^n - T_{\text{f},i}^{n-1}}{\Delta t} = -w_i^n v_i^n \frac{T_{\text{f},i}^n - T_{\text{f},i-1}^n}{\Delta x} + \frac{2\alpha_{\text{T},i}^n}{\rho_{\text{f}} c_{\text{f}}} \left[T_{\text{fw},i}^n - T_{\text{f},i}^n \right] \tag{23}$$

$$\frac{T_{\text{fw},i}^{n+1} - T_{\text{fw},i}^n}{\Delta t} = \frac{1}{\delta_i^{n+1}} \left[\lambda_i \left(T_{\text{f},i}^{n+1} - T_{\text{fw},i}^{n+1} \right) + \varphi_i \left(T_{\text{res}} - T_{\text{f},i}^{n+1} \right) \right] \tag{24}$$

$$\begin{aligned} v_i^n &= \frac{0.5 Q_k \Delta t - \Delta x h \sum_{m=1}^{j-1} 2 V_{\text{l},m}^n \Delta t_m}{\Delta t h w_i^{n+1}}, \lambda_i = \left(\frac{\rho_{\text{f}} c_{\text{f}}}{(\rho c)_{\text{eff}}} V_{\text{leak},i}^{n+1} + \frac{\alpha_{\text{T},i}^{n+1}}{(\rho c)_{\text{eff}}} \right), \\ \varphi_i &= \frac{\mathrm{e}^{-\frac{C^2}{D}}}{1 + \operatorname{erf}\left(\frac{\mathrm{C}}{\sqrt{\mathrm{D}}} \right)} \frac{D}{\sqrt{\pi D \varsigma_i}}, \quad \delta_i^{n+1} = C_{\text{leak}} \sqrt{(n+1)\Delta t - \tau_{x,i}}, \\ V_{\text{leak},i}^{n+1} &= \frac{C_{\text{leak}}^i}{\sqrt{(n+1)\Delta t - \tau_{x,i}}}, \quad \alpha_{\text{T},i}^{n+1} = \frac{k_{\text{f}} N_{\text{u}}}{w_i^{n+1}}, C = \frac{\rho_{\text{f}} \mathrm{c}_{\text{f}}}{(\rho c)_{\text{eff}}} C_{\text{leak}}^i, \quad D = \frac{k_{\text{eff}}}{(\rho c)_{\text{eff}}} \end{aligned} \tag{25}$$

The energy equation for the near-fracture formation is discretized using the Crank-Nicolson finite difference scheme, and the resulting difference equation is given as follows:

$$\frac{T_{\mathrm{r},j}^{n+1}-T_{\mathrm{r},j}^{n}}{\Delta t}=\frac{k_{\mathrm{eff}}}{2(\rho c)_{\mathrm{eff}}}\left[\frac{T_{\mathrm{r},j+1}^{n}-2T_{\mathrm{r},j}^{n}+T_{\mathrm{r},j-1}^{n}}{(\Delta y)^{2}}+\frac{T_{\mathrm{r},j+1}^{n+1}-2T_{\mathrm{r},j}^{n+1}+T_{\mathrm{r},j-1}^{n+1}}{(\Delta y)^{2}}\right]$$
$$-\frac{\rho_{\mathrm{f}}c_{\mathrm{f}}}{2(\rho c)_{\mathrm{eff}}}V_{\mathrm{leak},i}^{n+1}\left[\frac{T_{\mathrm{r},j+1}^{n}-T_{\mathrm{r},j-1}^{n}}{2\Delta y}+\frac{T_{\mathrm{r},j+1}^{n+1}-T_{\mathrm{r},j-1}^{n+1}}{2\Delta y}\right] \tag{26}$$

The fracture propagation model established in this paper is a typical thermo-hydro-mechanical (THM) coupling model, which is solved using a fully coupled implicit approach. Parameter transfer is employed to facilitate the coupling between the temperature field and the fluid-solid field. It is important to note that the fluid viscosity, the comprehensive fluid loss coefficient, and the thermal stress acting on the fracture elements all depend on the solution of the temperature field. Once the fluid pressure, fracture width, temperature-dependent thermal stress, and viscosity are obtained from the fluid-solid field, these quantities are exchanged with the temperature field via parameter transfer. A fully coupled implicit iteration is then performed until convergence of the transferred parameters is achieved. More detailed description of the solution procedure can be referred to the literature [20].

3 Model validation

To validate the accuracy of the developed code, numerical simulations of fracture propagation in the viscosity-dominated regime were performed. The temperature of the fracturing fluid at the fracture inlet was set to 30 °C, while the formation temperature was set to 115 °C. The thermal expansion coefficient of the formation rock was taken as 7×10^{-6} m/(m·°C) (or simply per °C), and the fluid loss coefficient of the fracturing fluid was 1×10^{-5} m·s$^{-0.5}$. The basic parameters for fracture propagation are provided in the literature [20], and the parameters for temperature distribution calculation are listed in Table 2. Figure 5 compares the results obtained from the developed code (for temperature differences between the fracturing fluid and the initial formation temperature, ΔT = 0 °C and ΔT = 85 °C) with the analytical solutions for viscosity-dominated (M-solution) fracture propagation in the KGD model given by Adachi[21]和 Detounay[22].

As shown in Fig. 4, the numerical results for viscosity-dominated propagation without considering thermal stress are in good agreement with the corresponding

analytical solutions, demonstrating the reliability of the developed code in simulating dynamic fracture propagation. Fig. 4 also presents the results obtained when thermal stress is taken into account. Compared to the case without thermal stress, the fracture aperture at the inlet becomes wider while the fracture half-length becomes shorter. These observations are consistent with the conclusions reported in the literature [23], thereby indirectly confirming the reliability of the computational results.

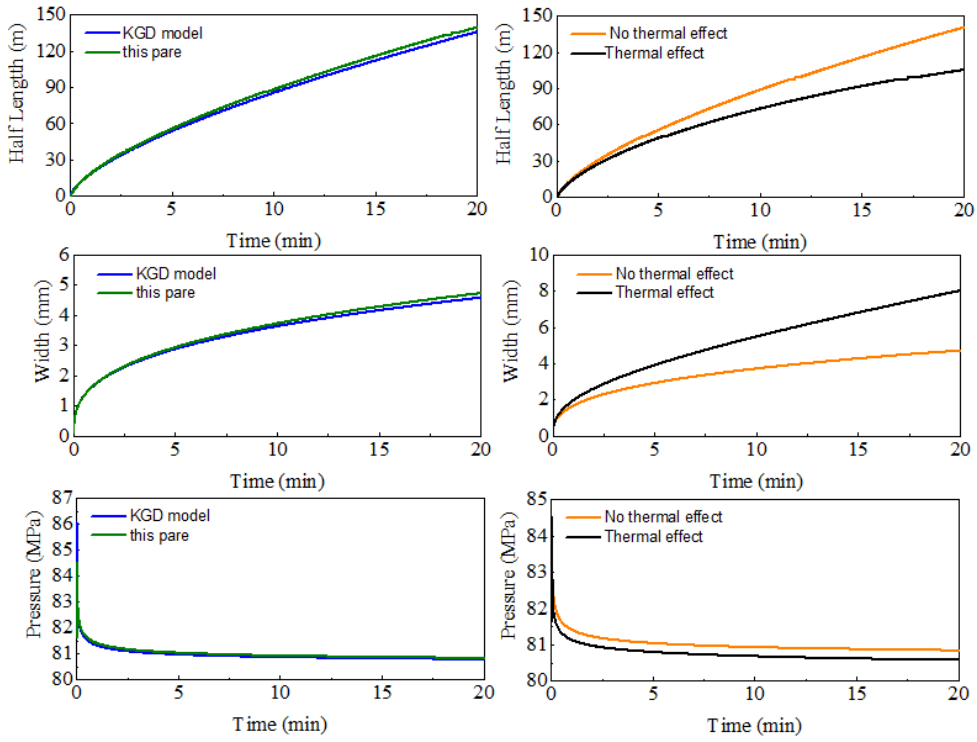


Fig. 4 Comparison of KGD fracture analytical solution with the results of this paper (top); comparison of numerical solutions of this paper with and without thermal effects (bottom).

To further verify that the constructed fracture propagation model can accurately and effectively simulate the fracture morphology of multiple fractures propagating simultaneously, the computational results from the non-planar fracture propagation model presented by Wu et al. [24] were adopted as a reference, and the basic parameters required for the calculations were taken from Table 1 of the reference [24]. Fig. 5 presents the simulated fracture morphology of dual-fracture synchronous propagation under horizontal stress differences of 0 MPa and 0.9 MPa, respectively. In the case without considering thermal effects, the simulated fracture results are in good agreement with those reported in the literature, whereas when thermal effects are considered, the fracture length is slightly shorter than the numerical results of Wu et al. [24]. This is because the simulation time is relatively short and the thermal effects are not significant; hence, the difference between the two cases is minimal. In summary,

through comparison with the analytical solution and the multi-fracture numerical solution, the accuracy of the fracturing model constructed in this study is verified, demonstrating its capability to simulate non-planar fracture propagation behavior.

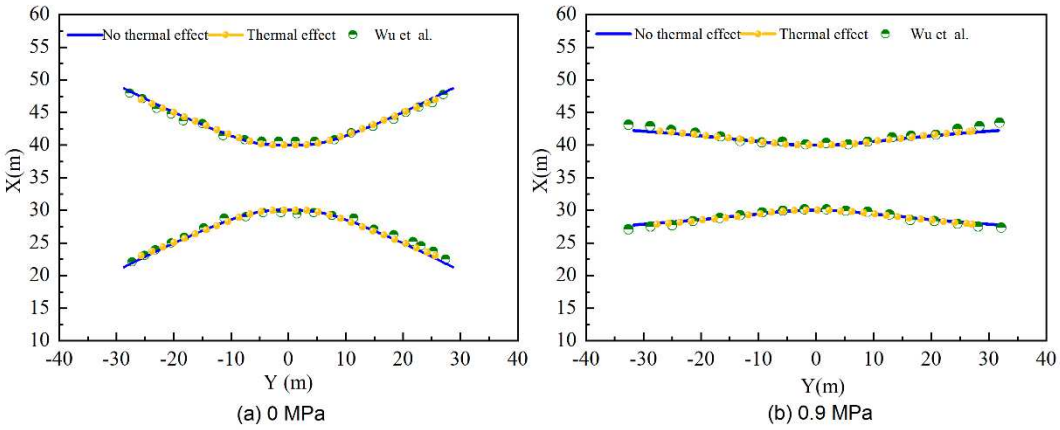
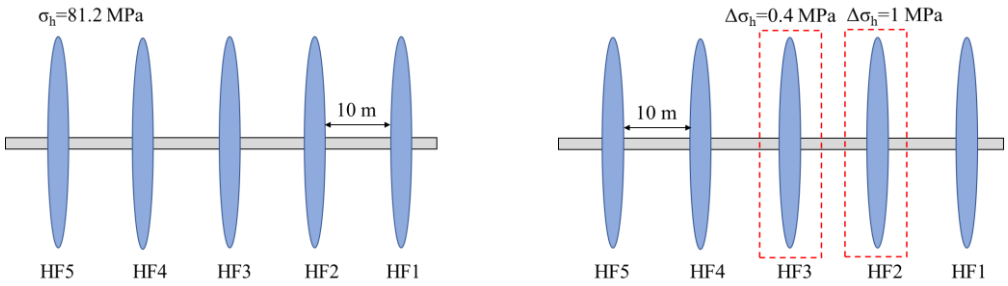


Fig. 5 Comparison of Simulated Fracture Morphology under Different Horizontal Stress Differences.

4 Results and Discussion

Taking a deep shale gas well in southeastern Sichuan as an example, a fracturing model was constructed to reveal the propagation laws of multi-cluster limited-entry perforation fractures under thermal effects. The target reservoir depth of this well is 3650 m, with a formation temperature of 115.6°C and a casing size of 5½ inches. The fracturing fluid injected at the wellhead has a temperature of 25°C. The main simulation parameters are listed in Table 2. It should be noted that the temperature calculation parameters involved from the wellhead to the bottom of the well and its specific calculation methods for the temperature are provided in reference [14]. Considering the potential non-uniform stress distribution in deep shale gas sections, both uniform and non-uniform in-situ stress models were established based on typical in-situ stress data from deep shale gas wells. The fracture numbering and their relative positions to the horizontal wellbore are shown in Fig. 6. To quantitatively analyze the impact of thermal effects on dynamic fracture propagation, the dimensionless fracture length is defined as the ratio of the length of each cluster fracture to the total length of all fractures. The standard deviation of fluid intake ratio (Q_{sd}) and the coefficient of variation of dimensionless fracture length (L_{cv}) are used to quantify the heterogeneity of multi-cluster fracture propagation.



(a) Uniform in-situ stress model **(b) Non-uniform in-situ stress model**

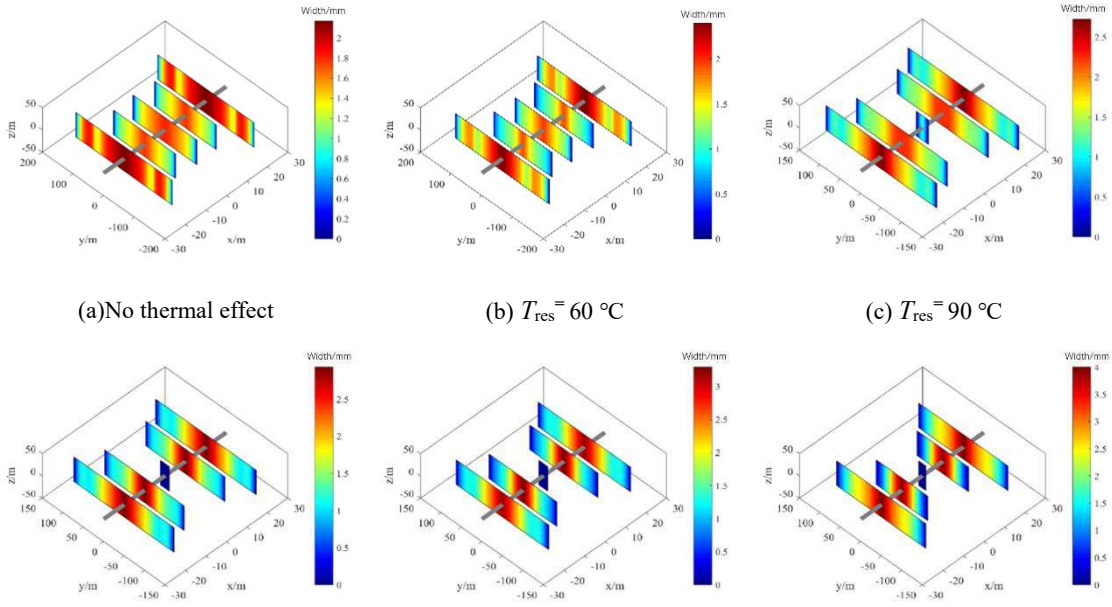
Fig. 6 Schematic of fracture numbering and in-situ stress distribution model

Tab. 2 Basic parameters of fracture propagation simulation

Parameters	Unit	Value	Parameters	Unit	Value
Minium Horizontal stress	MPa	81.2	Cluster spacing / m	m	10
Horizontal stress contrast	MPa	6	perforations per cluster		16
Yong's Module，	GPa	25	Perforation diameter	mm	11.4
Poisson's ratio		0.25	Perforation abrasion coefficient		0.85
Type I fracture toughness	$MPa \cdot m^{0.5}$	1.5	Wellbore inner diameter	mm	138.2
Type II fracture toughness	$MPa \cdot m^{0.5}$	3	Pumping rate，	m^3/min	12
Filtration coefficient，	$10^{-4} m/min^{0.5}$	1.6	Fracture height	m	55
Fracturing fluid viscosity	mPa·s	10	Thermal expansion coefficient	$10^{-6}/K$	1.0
Temperature sensitivity coefficient of fracturing fluid	1/℃	0.02			

Formation temperature is one of the factors affecting the propagation of multi-cluster fractures, as it influences the viscosity of injected fluids, fluid loss characteristics, heat exchange efficiency, and temperature distribution within the formation. Using the parameters in Table 2 and varying only the formation temperature, simulations were conducted to analyze fracture geometries under different formation temperatures, with the in-situ stress model shown in Fig. 6a. As illustrated in Fig. 7, with increasing formation temperature, fracture length decreases, overall fracture width increases, and the geometric differences among multi-cluster fractures become more pronounced. For example, at a formation temperature of 60°C, the lengths of the outer fractures (HF1 and HF5) and inner fractures (HF2 and HF4) are 150 m and 92 m, respectively, with fracture mouth widths of approximately 2.4 mm. In contrast, at a formation temperature of 150°C, the lengths of the outer and inner fractures decrease to 110 m and 80 m, respectively, while the fracture mouth width increases to about 3.2 mm. The results in Fig. 8 and 9 explain the reasons for these changes. On one hand, higher formation temperatures lead to a reduction in fluid viscosity (the minimum viscosity decreases from 5 mPa·s to 1 mPa·s), which

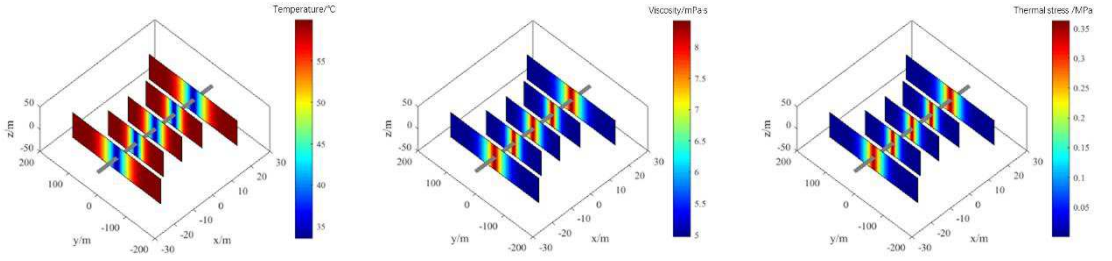
increases fluid loss and results in shorter fracture lengths. On the other hand, elevated formation temperatures enhance heat exchange efficiency, causing a rapid decline in temperature near the fractures and an increase in tensile thermal stress (the maximum thermal stress rises from 0.35 MPa to 1.6 MPa), thereby increasing fracture width. Additionally, according to the Displacement Discontinuity Method (DDM) proposed by Crouch [15], the increase in effective fracture opening leads to a greater range and magnitude of stress shadow effects, which also explains the subsequent phenomena of uneven fluid intake and propagation in multi-fracture systems.



(a)No thermal effect (b) T_{res}= 60 ℃ (c) T_{res}= 90 ℃

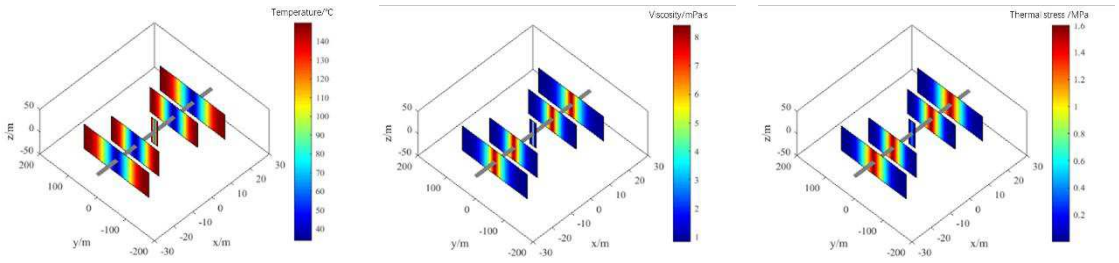
(d) T_{res}= 120 ℃ (e) T_{res}= 150 ℃ (f) T_{res}= 180 ℃

Fig. 7 Comparison of Fracture Width Profiles at Different Formation Temperatures



(a) Liquid temperature inside the fracture (b) Viscosity of liquid inside the fracture (c) Thermal stress on the fracture wall

Fig. 8- Simulation results when T_{res}= 60℃



(a) Liquid temperature inside the fracture

(b) Viscosity of liquid inside the fracture

(c) Thermal stress on the fracture wall

Fig. 9 Simulation results when T_{res}= 150°C

As shown in Fig. 10, higher formation temperatures lead to increased coefficient of variation L_{cv} and standard deviation of fluid intake ratio Q_{sd}. When the formation temperature rises from 60°C to 180°C, L_{cv} increases from 0.28 to 0.61, and Q_{sd} increases from 6.82% to 12.29%, indicating that elevated formation temperatures intensify the heterogeneity of multi-cluster fracture propagation. This demonstrates that high formation temperatures constrain uniform fracture propagation among clusters, though the underlying mechanism differs from the poroelastic effects that exacerbate propagation heterogeneity [25].

Furthermore, comparing results without thermal effects to those at 60°C formation temperature reveals similar fracture morphologies and fluid intake distributions. Based on a geothermal gradient of 0.025°C/m, a formation temperature of 60°C corresponds to a depth of 2400 m, which falls within the shallow formation range. This suggests that thermal effects may be neglected in fracture design for formations with temperatures below 60°C. However, as fracturing operations extend to deep and ultra-deep formations (where formation temperatures exceed 90°C), engineers should prioritize the impact of temperature variations on fluid properties and dynamic fracture propagation in fracture design optimization.

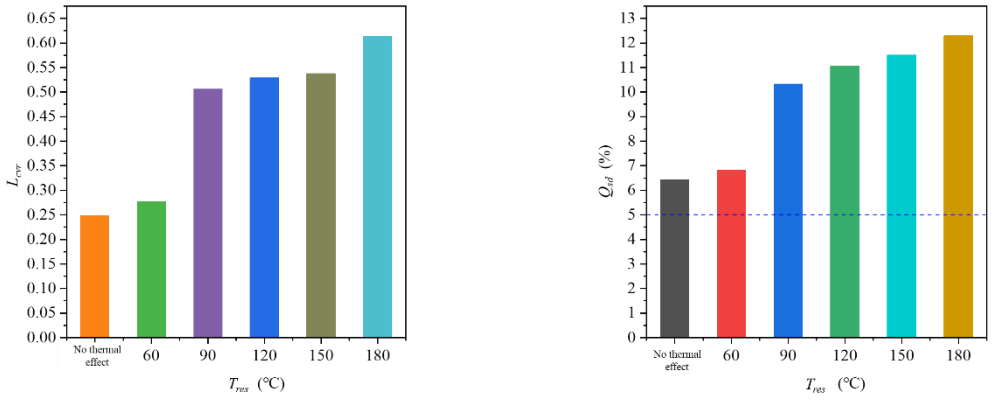
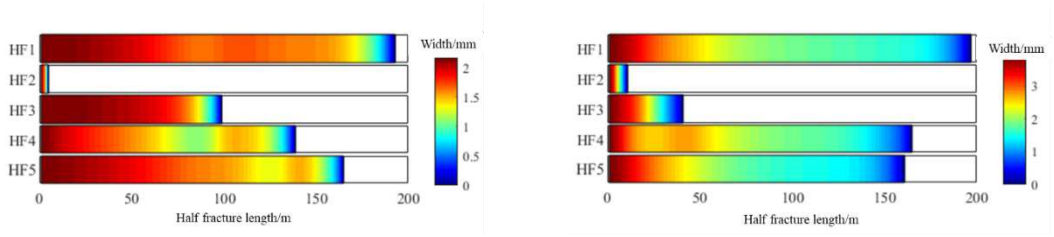


Fig. 10 Comparison of dimensionless length variation coefficient and liquid intake ratio standard deviation at different formation temperatures

4.1 The Influence of Perforation Number on Dynamic Fracture Propagation

Fig. 11 displays the multi-cluster fracture geometries with and without thermal effects, simulated using the non-uniform in-situ stress model shown in Fig. 6b, with 16 perforations per cluster. In both cases, perforation cluster HF2 located in the high-stress zone (1.0 MPa) within the stage is ineffective, while perforation cluster HF3 in the 0.4 MPa high-stress zone propagates. The difference lies in the fact that thermal stress promotes fracture width increase, resulting in stronger stress interference between fractures under thermal effects, making HF3 relatively more constrained. The calculated bottom-hole pressures for fracturing with and without thermal effects are 83.6 MPa and 84 MPa, respectively. The average perforation friction per cluster is 0.70 MPa and 0.73 MPa, respectively. Evidently, the perforation friction of less than 1 MPa fails to counteract the effects of non-uniform stresses (including non-uniform in-situ stress and stress shadow), leading to severe non-uniform fracture propagation in both cases, with length variation coefficients L_{cv} as high as 0.742 and 0.624, respectively.



（a）Without thermal effect　　（b）With thermal effect

Fig. 11 Fracture morphology with 16 perforation holes per cluster

Based on the limited-entry perforation concept, the number of perforations per cluster was gradually reduced from 16 until multi-cluster fractures achieved balanced propagation (or until the limited-entry condition was reached). Fig. 12 and 13 present the multi-cluster fracture geometries for perforation numbers of 10, 8, 6, and 4 under both scenarios, respectively.

It can be observed that the differences in fracture length and width among clusters decrease as the number of perforations increases. With 10 perforations per cluster, under the ideal scenario without thermal effects, the high-stress perforation cluster HF4 begins to initiate and propagate, though with limited extension of only about 25 m. In contrast, when thermal effects are considered, HF2 extends only about

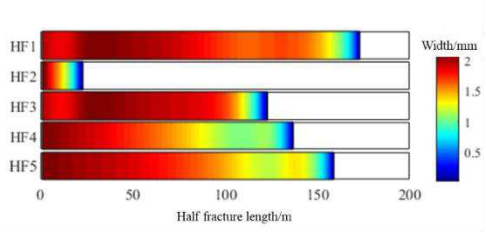
10 m. The bottom-hole pressures for the two scenarios are 85 MPa and 84.9 MPa, respectively, with average perforation friction values of 1.6 MPa and 1.72 MPa per cluster, and length variation coefficients (L_{cv}) of 0.49 and 0.54, respectively.

When the number of perforations is reduced to 6 per cluster, all perforation clusters initiate in both scenarios, but differences in fracture length remain. For instance, in the scenario without thermal effects, cluster HF1 has the longest fracture length with a half-length of 140 m, while HF2 has the shortest at only 86 m. At this point, the average perforation friction reaches 3.3 MPa.

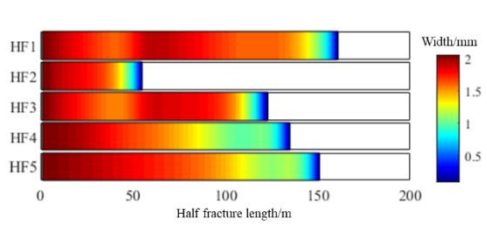
Further reducing the number of perforations to 4 per cluster results in nearly consistent fracture widths and lengths across all clusters in both scenarios, with length variation coefficients (L_{cv}) approaching 0.1 and the average perforation friction increasing to 7.35 MPa.

This demonstrates that limited-entry perforation, particularly extreme limited-entry perforation, can increase perforation friction, thereby mitigating the uneven propagation caused by heterogeneous in-situ stress, stress shadow effects, and thermal effects within the stage. In geological formations with heterogeneous in-situ stress, high stress within the stage is the dominant factor leading to uneven multi-cluster fracture propagation.

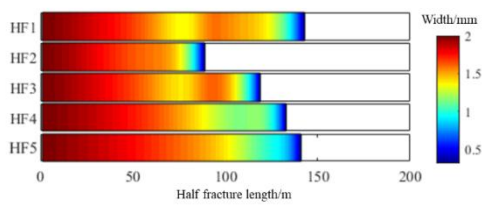
When thermal effects are not considered, increasing the perforation friction to 1.6 MPa can enable fractures to overcome an additional 1 MPa of compressive stress and initiate. However, to achieve balanced propagation, the perforation friction must be increased to at least 3.3 MPa. When thermal effects are considered, the required perforation friction is relatively higher.



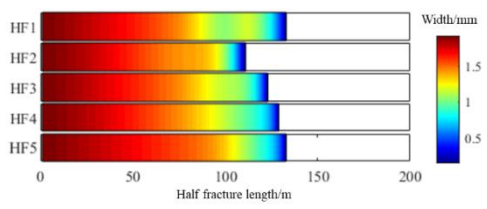
(a) 10 perforation holes per cluster



(b) 8 perforation holes per cluster

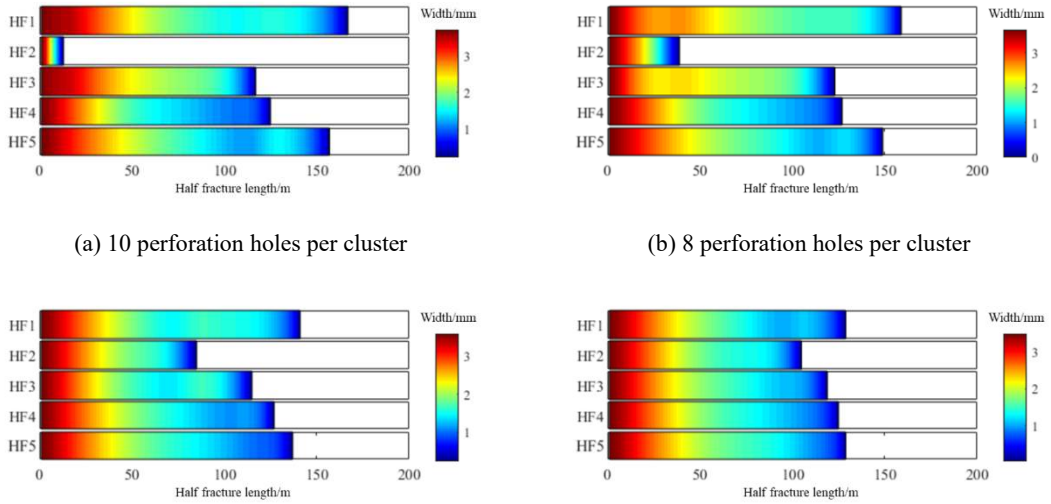


(c) 6 perforation holes per cluster



(d) 4 perforation holes per cluster

Fig. 12 Fracture morphology under different numbers of perforations without considering thermal effects



(a) 10 perforation holes per cluster

(b) 8 perforation holes per cluster

(c) 6 perforation holes per cluster

(d) 4 perforation holes per cluster

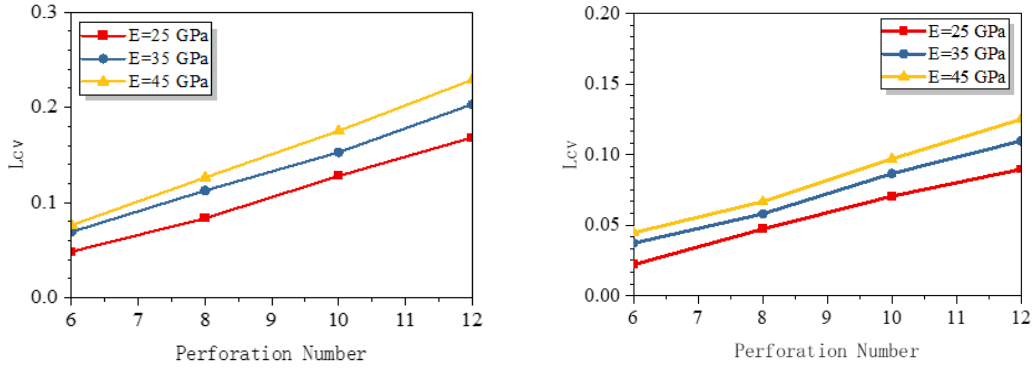
Fig. 13 Fracture morphology under different numbers of perforations with considering thermal effects

4.2 Optimization of Perforation Design under Different Young's Modulus and Flow Rate Conditions

Young's modulus and treatment rate significantly influence the non-uniform propagation of multi-cluster fractures. Using the two in-situ stress models established in Fig. 6 and taking the fracture length variation coefficient as the optimization objective, this section discusses the optimal number of perforations required to achieve balanced multi-cluster fracture propagation under different Young's modulus values and treatment rates through 60 simulation cases. It should be noted that a dimensionless length variation coefficient (L_{cv}) of less than 0.2 is used as the criterion for judging balanced multi-fracture propagation in this study.

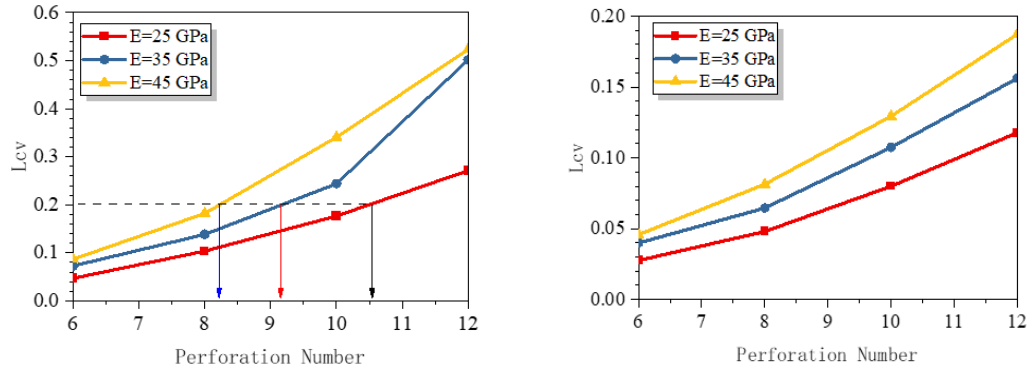
Uniform In-Situ Stress Distribution. In Fig. 6a, the minimum horizontal principal stress is identical for all clusters, at 81.2 MPa. Fluid distribution among clusters is controlled by perforation friction, flow friction, and fracture interference. As shown in Fig. 14, without considering thermal effects, at a treatment rate of 12 m^3/min and a Young's modulus ranging from 25 to 35 GPa, the optimal number of perforations is 12 per cluster. However, when the Young's modulus is 45 GPa, the optimal number decreases to 11 per cluster. When the treatment rate is increased to 18 m^3/min, the optimal number of perforations remains 12 per cluster across the Young's modulus range of 25 to 45 GPa.

As shown in Fig. 15, when thermal effects are considered, at a design treatment rate of 12 m³/min, the optimal number of perforations for limited-entry fracturing decreases with increasing Young's modulus. When Young's modulus increases from 25 GPa to 45 GPa, the optimal number of perforations decreases from 10 to 8 per cluster. At a design treatment rate of 18 m³/min, the optimal number of perforations remains 12 per cluster for all Young's modulus values.



(a) 12 m³/min (b) 18 m³/min

Fig. 14 Number of perforations vs. coefficient of variation of length under different Young's modulus

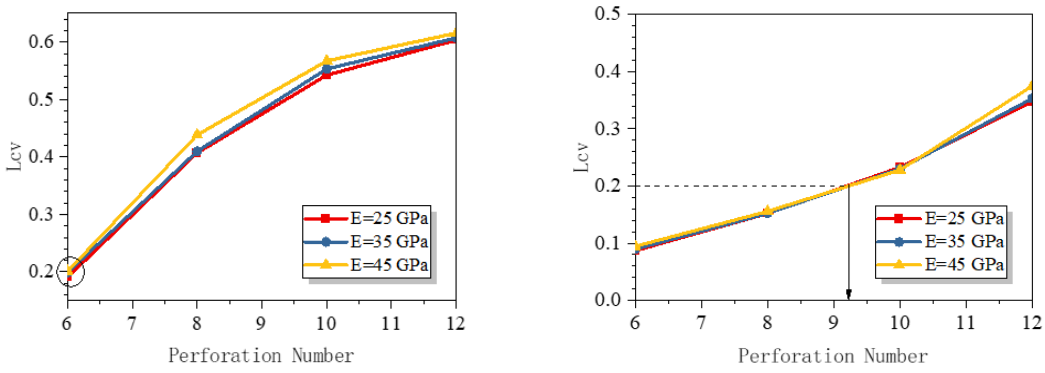


(a) 12 m³/min (b) 18 m³/min

Fig. 15 Number of perforations vs. coefficient of variation of length under different Young's modulus with thermal effects

A comparison with scenarios neglecting thermal effects reveals that at low flow rates, thermal effects make the optimal perforation count in limited-entry fracturing more sensitive to variations in Young's modulus. However, when the flow rate is increased beyond a certain threshold, the optimal perforation count shows no significant change with variations in Young's modulus. Under both scenarios (with and without thermal effects), the optimal perforation counts converge, indicating that increasing the flow rate can partially mitigate the negative impact of thermal effects on balanced multi-cluster propagation.

Non-uniform In-situ Stress Distribution. The optimal perforation count under thermal effects is generally less than or equal to that under ideal conditions without thermal considerations. Consequently, a perforation design satisfying the former scenario can also be applied to the latter. Therefore, Fig. 16 only presents the relationship between the designed perforation count and the fracture length variation coefficient for different Young's modulus values under thermal effects. When the treatment rate is 12 m^3/min, the perforation count required to achieve a length variation coefficient below 0.2 is 6, making this the optimal perforation count under these conditions. At a treatment rate of 18 m^3/min, the optimal perforation count for balanced cluster propagation is approximately 9 perforations per cluster. Furthermore, it can be observed that when the minimum horizontal stress difference within the stage is 1 MPa, although the fracture length variation coefficient varies with Young's modulus, adjusting the perforation count to balance the 1 MPa stress difference simultaneously resolves the non-uniform propagation of multi-cluster fractures across different Young's modulus values. Additionally, similar to the uniform in-situ stress distribution scenario, the optimal perforation count increases with higher treatment rates.



(a) 12 m^3/min (b) 18 m^3/min

Fig. 16 Relationship between the number of perforations and the coefficient of variation of length under different Young's modulus values when considering thermal effects

5 Conclusion

This study developed and validated a numerical model for non-planar fracture propagation in multi-cluster staged fracturing of deep shale formations, incorporating thermal effects. Based on this model, the propagation behavior of multi-cluster fractures under high-temperature conditions was revealed, and the influence of limited-entry perforation on fracture extension was analyzed. The main conclusions

are as follows:

(1) Thermal effects exacerbate the non-uniform propagation of multi-cluster fractures. When the formation temperature exceeds 90°C, the impact of thermal effects on fracture propagation must be considered. Higher formation temperatures intensify thermal effects, leading to greater disparities in fluid intake and fracture geometry among clusters.

(2) Reducing the number of perforations to increase perforation friction can mitigate non-uniform propagation caused by heterogeneous in-situ stress, stress shadow effects, and thermal effects within the stage. Under ideal conditions without thermal effects, increasing perforation friction to 1.6 MPa enables fractures to overcome an additional 1 MPa of compressive stress for initiation and extension. To achieve further balanced propagation, the required perforation friction must be raised to at least 3.3 MPa. When thermal effects are considered, the required perforation friction is even higher.

(3) At low flow rates, thermal effects amplify the influence of Young's modulus on the optimal perforation count. Increasing the flow rate can relatively mitigate the negative impact of thermal effects on balanced fluid distribution among clusters. Under uniform in-situ stress distribution and considering thermal effects, at a flow rate of 12 m^3/min, the optimal perforation count for limited-entry fracturing decreases from 10 to 8 perforations per cluster as Young's modulus increases from 25 GPa to 45 GPa. When the flow rate is increased to 18 m^3/min, the optimal perforation count rises to 12 perforations per cluster.

Authorship contribution statement

Hao Jiang: methodology, software, validation, formal analysis, investigation, resources, data curation, visualization, writing—original draft preparation, writing—review and editing, funding acquisition; **Jianfeng Xiao:** methodology, software, validation, formal analysis, supervision; **Wei Jiang:** conceptualization, methodology, supervision, project administration; **Liang Yang:** formal analysis, software, writing—original draft preparation; **Lan Ren:** conceptualization, methodology, resources, writing—review and editing, funding acquisition; **Cai Deng:** formal analysis, software; **Dengji Tang:** writing—original draft preparation, writing—review and editing. **Longqing Zou**: data curation.
All authors have read and agreed to the published version of the manuscript.

Declaration of Competing Interest

The authors declare that they have no known competing financial interests or personal relationships that could have appeared to influence the work reported in this paper.

Data Availability Statement

Part of the data used and/or analyzed during the current study is available from a supplementary file and the other part is available from the corresponding author on reasonable request.

Acknowledgments

This work is supported by National Natural Science Foundation of China (No. U21B2071) and Youth Science and Technology Innovation Fund of CNPC (No. 2024DQ03068). Thanks for their support for this article.

References

[1] Miller C, Waters G, Rylander E. Evaluation of production log data from horizontal wells drilled in organic shales[R]. SPE 144326, 2011.
[2] Ghassemi A, Zhou X. A three-dimensional thermo-poroelastic model for fracture response to injection/extraction in enhanced geothermal systems[J]. Geothermics, 2011, 40(1):39-49.
[3] Wang Y. Fracture initiation and thermal cracking process during EGS in geothermal reservoir[C]//52nd U.S. Rock Mechanics/Geomechanics Symposium. American Rock Mechanics Association, Seattle, 2018.
[4] Lu Y, Cha M. Thermally induced fracturing in hot dry rock environments-Laboratory studies[J]. Geothermics, 2022, 106: 102569.
[5] Abdollahipour A, Marji M F. A thermo-hydromechanical displacement discontinuity method to model fractures in high-pressure, high-temperature environments[J]. Renewable Energy, 2020, 153: 1488-1503.

[6] Tarasovs S, Ghassemi A. Radial cracking of a borehole by pressure and thermal shock[C]//46th U.S. Rock Mechanics/Geomechanics Symposium. American Rock Mechanics Association, 2012.
[7] Li W, Soliman M, Han Y. Investigation of Thermal Effects of Fluid Injection into Unconsolidated Formation in Microscopic Numerical Models[C]//50th U.S. Rock Mechanics/Geomechanics Symposium. American Rock Mechanics Association, Houston, 2016.
[8] Salimzadeh S, Paluszny A, Zimmerman R. Thermal effects during hydraulic fracturing in low-permeability brittle rocks[C]//50th U.S. Rock Mechanics/ Geomechanics Symposium, American Rock Mechanics Association, Houston, 2016.
[9] Bazargan M, Broumand P, Gudmundsson A, et al. Investigating the Role of Temperature on Thermal Stress and Fracture Propagation in Geothermal Systems[C]//51st U.S. Rock Mechanics/Geomechanics Symposium. American Rock Mechanics Association, San Francisco, 2017.
[10] Luo Z, Cheng L, Zhao L, et al. Numerical simulation and analysis of thermo-hydro-mechanical behaviors of hydraulic fracturing in naturally fractured formation using a THM-XFEM coupling model[J]. Journal of Natural Gas Science and Engineering, 2022, 103: 104657.
[11] Liu W, Zeng Q, Yao J. Numerical simulation of elasto-plastic hydraulic fracture propagation in deep reservoir coupled with temperature field[J]. Journal of Petroleum Science and Engineering, 2018, 171: 115-126.
[12] Valkó P, Economides M J. Hydraulic fracture mechanics[M]. Chichester: Wiley, 1995.
[13] Cohen C E, Weng X, Kresse O. Influence of fracturing fluid and reservoir temperature on production for complex hydraulic fracture network in shale gas reservoir[R]. SPE 167097, 2013.
[14] Kamphuis H, Davies D R, Roodhart L P. A new simulator for the calculation of the in situ temperature profile during well stimulation fracturing treatments[J]. Journal of Canadian Petroleum Technology, 1993, 32(05): 38-47.
[15] Crouch S. Solution of plane elasticity problems by the displacement discontinuity method. I. Infinite body solution[J]. International Journal for Numerical Methods in Engineering, 1976, 10(2): 301-343.
[16] Olson J E. Predicting Fracture Swarms—The Influence of Subcritical Crack Growth and the Crack-Tip Process Zone on Joint Spacing in Rock[M]. Geological Society of London Special Publication: 73–87, 2004.
[17] Zhuang D, Yin T, Li Q, et al. Effect of injection flow rate on fracture toughness during hydraulic fracturing of hot dry rock (HDR)[J]. Engineering Fracture Mechanics, 2022, 260: 108207.
[18] Collin M, Rowcliffe D. Analysis and prediction of thermal shock in brittle materials[J]. Acta materialia, 2000, 48(8): 1655-1665.
[19] Shen B, Stephansson O. Modification of the G-criterion of crack propagation in

compression[J]. International Journal of Engineering Fracture Mechancis,1993, 47(2):177–189.
[20] Lin R, Peng S R, Zhao J Z, et al. Multiple hydraulic fracture propagation simulation in deep shale gas reservoir considering thermal effects[J]. Engineering Fracture Mechanics, 2024, 303: 110147.
[21] Adachi J I. Fluid-driven fracture in permeable rock[D]. University of Minnesota, 2001.
[22] Detournay E. Propagation Regimes of Fluid-Driven Fractures in Impermeable Rocks[J]. International Journal of Geomechanics, 2004, 4(1):35-45.
[23] Zeng Q D, Yao J, Shao J F. An extended finite element solution for hydraulic fracturing with thermo-hydro-elastic–plastic coupling[J]. Computer Methods in Applied Mechanics and Engineering, 2020, 364: 112967.
[24] Wu R, Kresse O,Weng X, et al. Modeling of interaction of hydraulic fractures in complex fracture networks[R]. SPE 152052, 2012.
[25] Dontsov E V. An efficient computation of leak-off induced poroelastic stress for a hydraulic fracture[J]. Journal of the Mechanics and Physics of Solids, 2021, 147: 104246.

Supplementary Files

This is a list of supplementary files associated with this preprint. Click to download.

- PartDataset.rar